Plenoptic imaging through correlation

F. Di Lena[1][2] (*) on behalf of F. V. Pepe[2], A. Mazzilli[1],
A. Garuccio[1][2][3], G. Scarcelli[4] and M. D'Angelo[1][2][3]

[1] *Dipartimento Interateneo di Fisica, Università degli Studi di Bari - Bari, Italy*
[2] *INFN, Sezione di Bari - Bari, Italy*
[3] *Istituto Nazionale di Ottica (INO-CNR) - I-50125 Firenze, Italy*
[4] *Fischell Department of Bioengineering, University of Maryland - College Park, MD 20742, USA*

received 31 March 2018

Summary. — Traditional optical imaging is characterized by the typical trade-off between resolution and depth of field (DOF). In order to increase resolution, high numerical apertures (NA) are needed, but the associated large angular uncertainty results in a limited range of depths that can be put in sharp focus. Plenoptic imaging (PI) is a promising optical modality that simultaneously captures the location and the propagation direction of light in order to enable refocusing of the acquired images. Thanks to its ability to simultaneously acquire multi-perspective images, plenoptic imaging is one of the most promising technologies for 3D imaging. However, the improvement offered by standard plenoptic imaging is practical rather than fundamental: the increased DOF leads to a proportional reduction of the resolution well above the diffraction limit imposed by the lens NA. We have recently demonstrated that the intrinsic correlation of both chaotic light and entangled photons enables pushing plenoptic imaging to its fundamental limits of both resolution and DOF. In this paper we demonstrate correlation plenoptic imaging (CPI) of a double slit and present the comparison between theoretical prediction and experimental images.

1. – Introduction

Plenoptic imaging (PI) is a novel optical technique for recording visual information [1]. A plenoptic camera can record both the position and the propagation direction of light in a single shot, thus enabling refocusing and 3D imaging. The working principle of plenoptic imaging has many applications, from stereoscopy [1-3], to microscopy [4-7],

---

(*) E-mail: francesco.dilena@ba.infn.it

particle image velocimetry [8], particle tracking and sizing [9], wavefront sensing [10-13], as well as photography, where it enables digital cameras with refocusing capabilities [14, 15]. In particular, the capability of PI to simultaneously acquire multiple-perspective 2D images puts it among the fastest and most promising methods for 3D imaging with the available technologies [16]. In fact, high-speed and large-scale 3D functional imaging of neuronal activity has been demonstrated [7]. Furthermore, first studies for surgical robotics have been performed [17], together with endoscopic application [18] and blood-flow visualization [19].

The key component of a standard plenoptic camera is a microlenses array inserted in the native image plane, and playing the role of imaging pixels. The sensor plane captures the repeated images of the main camera lens formed by the microlenses [1, 15]. The image of the camera lens provides the angular information which enables, in post-processing, the reconstruction of the light path. Such directional information can be employed for refocusing different planes, changing the point of view and extending the depth of field (DOF) within the acquired image. However, there is a fundamental trade-off between spatial and angular resolution in standard plenoptic imaging: An accurate angular information requires big microlenses, but the size of the microlenses limits the image resolution. If we indicate by N_{tot} the total number of pixels per line on the camera sensor, by N_x the number of microlenses per line, and by N_u the number of pixels per line associated with each microlens, then $N_x N_u = N_{tot}$. Hence, N_u, which fixes the directional resolution, also determines the amount of sacrificed image resolution. In short, standard PI gives the same resolution and DOF one would obtain with a N_u times smaller NA. The final advantage is thus practical rather than fundamental, and is limited to the higher luminosity (hence SNR) of the final image, as well as in the parallel acquisition of multiperspective images.

Correlation plenoptic imaging (CPI) has recently been proposed for overcoming this fundamental limit [20]. The main idea is to exploit the second-order spatio-temporal correlation properties of light to perform spatial and angular detection on two distinct sensors: By using two correlated beams, from either a chaotic [20, 21] or an entangled photon source [22], high-resolution imaging can be performed on one sensor [23-28] while simultaneously obtaining the angular information on the second sensor. As a result, the relation between the spatial (N_x) and the angular (N_u) pixels per line, at fixed N_{tot}, becomes linear rather than hyperbolic: $N_x + N_u = N_{tot}$ [20].

We have recently presented the first experimental realization of CPI [29]. In order to perform a better comparison between theory and experiment, in this paper we analyze one-dimensional images of a double slit, and employ the experimental data to visualize the experimental correlation function both before and after refocusing. The plenoptic properties of the correlation function and the working principle of the refocusing algorithm will thus be directly observed from the experimental data. Furthermore, we will discuss the DOF enhancement of CPI, with respect to both standard imaging and conventional plenoptic imaging.

2. – Experimental setup and results

The experimental setup is reported in fig. 1. To better understand this scheme, let us recall its underlying phenomenon, namely, ghost imaging with chaotic light [26, 27]. The correlation measurement between each pixel of S_a and the whole sensor S_b enables retrieving the "ghost" image of the object on the plane of S_a. Such a ghost image is focused provided the distance z_a between the source and the sensor S_a is equal to
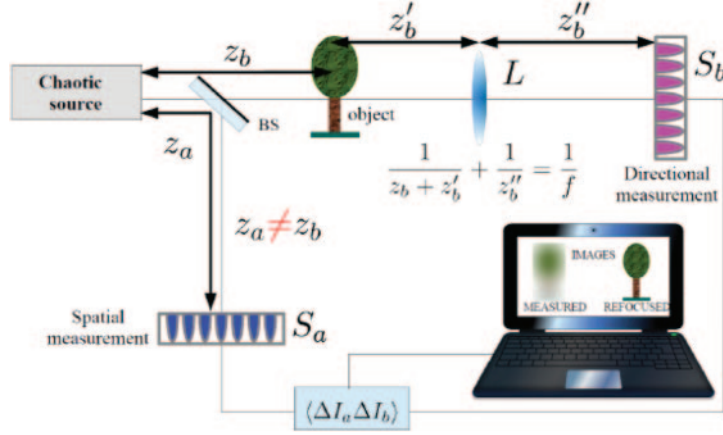
Fig. 1. – Schematic representation of the experimental setup employed for correlation plenoptic imaging [29]. Different from [29], here, S_a and S_b are scanning photodiodes connected to a fast oscilloscope. When measuring correlations of intensity fluctuations $\langle \Delta I_a \Delta I_b \rangle$, the chaotic light source acts as a focusing element and enables imaging the object on the plane of the (blue) sensor S_a. The light source is imaged by the lens L on the (red) sensor S_b to provide the angular information required for plenoptic imaging. The lens L thus replaces the whole microlens array of standard PI.

the distance z_b between the source and the object [26, 27]. Due to the spatio-temporal correlation properties of chaotic light, the light source plays the role of a focusing element, and replaces the lens of a standard imaging system with magnification $m = 1$ [27]. This justifies the name of *spatial sensor* for detector S_a, despite it detects a light beam that has never passed through the object. Similar to standard imaging, the maximum achievable resolution and DOF of a ghost image are defined by the NA of the focusing element (here, the chaotic light source), as seen from the object. In our case, $\Delta x^f = \lambda/\mathrm{NA} = 120\,\mu\mathrm{m}$ and, for objects at the resolution limit, $\mathrm{DOF} = \lambda/\mathrm{NA}^2 = 14.7\,\mathrm{mm}$. In the experiment, we have chosen a pixel size $\delta x = 50\,\mu\mathrm{m} \leq \Delta x^f/2$ that matches this resolution.

In order to understand how CPI enables increasing the depth of field of the acquired image and changing the viewpoint, let us now study the role of the high-resolution sensor S_b. Each pixel of this sensor corresponds to the source point from which the detected signal has been emitted. Correlation measurements between pixels of S_a and S_b thus enable tracking the "light ray" joining each object point (as retrieved by the ghost image on S_a) with each source point (as retrieved by S_b) [20, 21]. The high resolution of sensor S_b does not affect the retrieval of the ghost image of the object on S_a. The standard ghost image is recovered by summing the correlations between S_a and S_b over the whole sensor S_b, which thus corresponds to a "bucket" detector.

In our experiment, the resolution limit on the source image, as defined by the lens ($\lambda/\mathrm{NA}_L = 16\,\mu\mathrm{m}$), is smaller than the pixel size of S_b ($\delta u = 50\,\mu\mathrm{m}$). Thus, the resolution on the source plane is defined either by diffraction at the object or by the pixel size, namely $\Delta u = \max[\lambda z_b/a, 2\,\delta u/M]$, where $M = z_b''/(z_b + z_b')$ is the magnification of the lens [20].

We have employed double-slit masks as objects, thus mimicking small object details and easily monitoring the image resolution, both in the out-of-focus and in the refocused image. In fig. 2(a), (b), we report the experimental results obtained for a double-slit mask
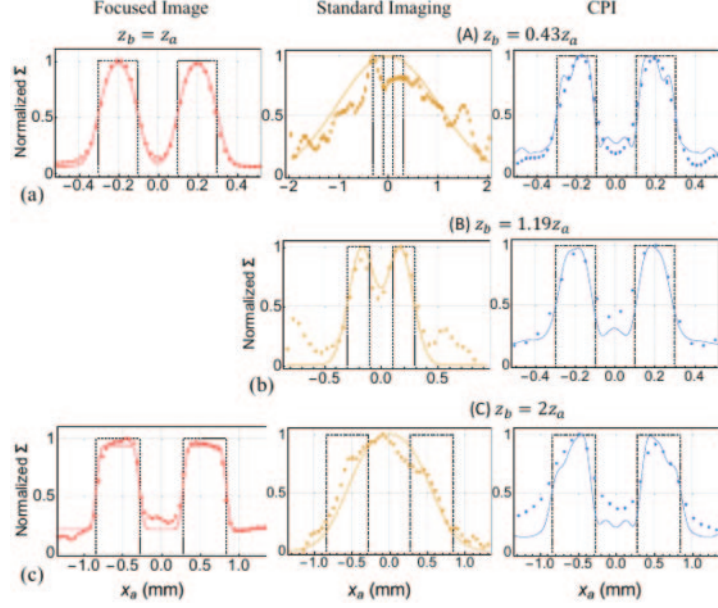
Fig. 2. – Comparison between the focused images (left column), the out-of-focus images (central column), and the refocused images (right column), as obtained in the setup of fig. 1 for two different double-slit masks: (a), (b) $a = 0.2\,\text{mm}$, $d = 2a$; (c) $a = 0.56\,\text{mm}$, $d = 2a$. Points indicate experimental data, the continuous curve is the theoretical prediction of eqs. (1) and (2), and the dashed line is the object mask.

with center-to-center distance $d = 0.40\,\text{mm} \lesssim 4\Delta x^f$ and slit width $a = d/2$. In the left column, we report the focused (ghost) image retrieved on S_a by measuring correlation with the whole detector S_b, when $z_b = z_a$. In the central column, we show the out-of-focus images obtained when the mask is moved out of the depth of field of the ghost image (as defined by the source numerical aperture), either closer (fig. 2(a)) or farther away (fig. 2(b)) from the source. In the right column, we report the correlation plenoptic images obtained by refocusing the corresponding out-of-focus images with the typical plenoptic algorithm [15], which in the case of CPI takes the form [20]:

$$(1) \qquad \Sigma^{\text{ref}}_{z_a,z_b}(\boldsymbol{\rho}_a) := \int \text{d}^2\boldsymbol{\rho}_b \Gamma_{z_a,z_b}\left(\frac{z_a}{z_b}\boldsymbol{\rho}_a - \frac{\boldsymbol{\rho}_b}{M}\left(1 - \frac{z_a}{z_b}\right), \boldsymbol{\rho}_b\right),$$

where

$$(2) \quad \Gamma_{z_a,z_b}(\boldsymbol{\rho}_a, \boldsymbol{\rho}_b) = \mathcal{K}\left|\int \text{d}\boldsymbol{\rho}_o A(\boldsymbol{\rho}_o) \int \text{d}\boldsymbol{\rho}_s \mathcal{S}(\boldsymbol{\rho}_s) e^{i\,k_z\left[\left(\frac{1}{z_b}+\frac{1}{z_a}\right)\frac{\rho_s^2}{2} - \left(\frac{\rho_o}{z_b} - \frac{\rho_a}{z_a}\right)\cdot\boldsymbol{\rho}_s - \frac{\rho_s\cdot\rho_b}{M\,z_b}\right]}\right|^2$$

represents the measured correlation of intensity fluctuations $\langle \Delta I_a \Delta I_b \rangle$ between point $\boldsymbol{\rho}_a$ on S_a and point $\boldsymbol{\rho}_b$ on S_b [20]. The functions $\mathcal{S}$ and A represent the transverse intensity profile of the source and the aperture function of the object, respectively. Unlike fig. 2(a), where the out-of-focus image is completely blurred, in fig. 2(b) the out-of-focus image can still be recognized. To better emphasize the refocusing power of CPI for
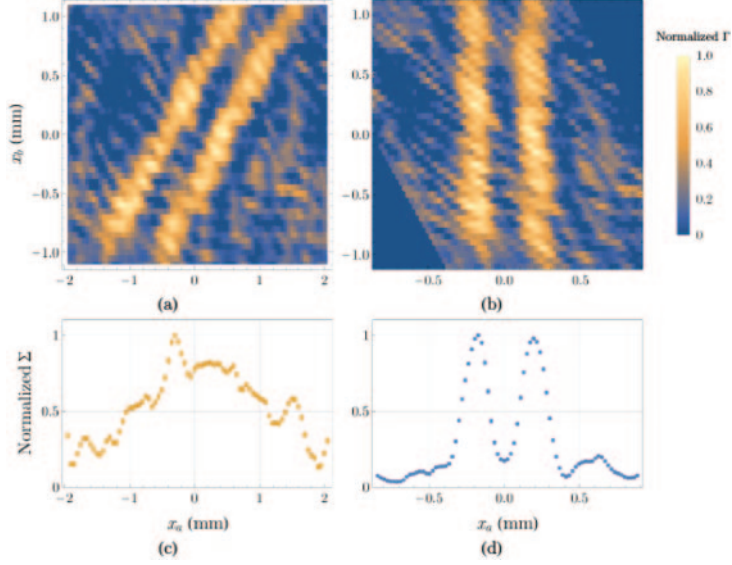
Fig. 3. – (a) Experimental results obtained by measuring the pixel-by-pixel spatio-temporal correlation between S_a and S_b, in the setup of fig. 1, with a double-slit mask having slit separation $d = 0.4\,\mathrm{mm}$ and slit width $a = d/2$, placed at a distance $z_b = 0.43 z_a$ from the source. (b) Result of the refocusing algorithm reported in the integrand of eq. (1), as applied to the raw data of panel (a). (c) Result of the integration over the angular sensor S_b of the raw data of panel (a), as one would get in standard ghost imaging. (d) Result of the integration over the angular sensor S_b of the refocused data of panel (b); this represents the final refocused image of CPI, as described by eq. (1).

distances $z_b > z_a$, we show in fig. 2(c) the result obtained with a larger object, having $d = 1.12\,\mathrm{mm} \simeq 9\Delta x^f$ and $a = d/2$. Both the refocusing capability of CPI, and the good agreement between experimental data (points) and theoretical prediction (solid line) are apparent in fig. 2. Notice that a constant fit of the background has been added to the theoretical prediction to take into account noise that is not included in our theory.

In fig. 3(a) we report the raw data obtained by measuring the pixel-by-pixel correlation of intensity fluctuations between S_a and S_b (*i.e.*, $\Gamma_{z_a,z_b}(\boldsymbol{\rho}_a, \boldsymbol{\rho}_b)$). For each pixel of the angular sensor S_b, we observe on S_a a displaced ghost image of the object: Hence, imaging the light source on the high-resolution sensor S_b enables changing the perspective on the observed scene[1]. This result explains why the standard ghost image reported in fig. 3(c) is blurred: When no angular information is retrieved (*i.e.*, when integration over S_b is performed), all displaced images overlap giving rise to the out-of-focus image $\Sigma_{z_a,z_b}(\boldsymbol{\rho}_a) = \int d^2\boldsymbol{\rho}_b\, \Gamma_{z_a,z_b}(\boldsymbol{\rho}_a, \boldsymbol{\rho}_b)$. In ghost imaging, the integration performed by the bucket detector clearly erases the precious information contained in the raw data of CPI. On the contrary, CPI exploits the extra information gained by the high resolution detector S_b. As shown in fig. 3(b), the reshaping and resizing algorithm that appears in

---

[1] The change of viewpoint is a common feature of both PI and CPI, with the only difference that, in CPI, it is obtained with a single lens (L) rather than by the microlens array typical of standard PI. Despite we do not use it in the present work, it is worth emphasizing the key role played by the change of perspective and its achievable resolution, for implementing 3D imaging.
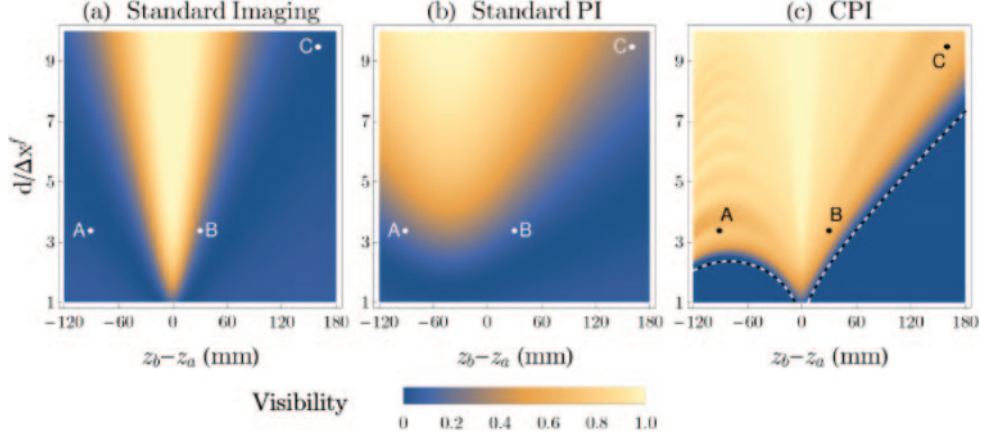
Fig. 4. – Analysis of the range of perfect refocusing for double-slit objects with $d = 2a$; the slit distance d is normalized to the resolution of the focused image Δx^f. The visibility is computed by considering (a) standard imaging, (b) standard plenoptic imaging (with $N_u = 3$), and (c) CPI devices sharing the same NA employed in the experiment. Points A, B and C correspond to the experimentally analyzed cases (fig. 2), while the (white) dashed line in panel (c) is the perfect-refocusing limit obtained by eq. (3).

the integrand of eq. (1) realigns all displaced images: no blurring occurs anymore upon integration over S_b, and the refocused image of fig. 3(d) is instead obtained.

3. – Comparison with standard imaging devices

In fig. 4(c), the dashed (white) line represents the geometrical-optics prediction for "perfect" refocusing in CPI [20]

$$(3) \qquad \left| 1 - \frac{z_a}{z_b} \right| < \frac{\Delta x}{\Delta u} = \frac{dz_a/z_b}{\max[\lambda z_b/a, 2\delta_u/M]}$$

with Δx the resolution on the sensor S_a, and Δu the resolution on the light source plane. Equation (3) enables to identify the physical quantities that define the spatial and the angular resolution of CPI, in the simple case of a double-slit object of width a and center-to-center distance $d = 2a$. In particular, the resolution Δx is defined by the geometrical projection of the image of the double slit on the sensor plane. On the other hand, the resolution Δu on the source plane is generally defined by diffraction at the object (*i.e.*, $\Delta u = \lambda z_b/a$); the pixel size δ_u only enters into play for objects extremely close to the light source (*i.e.*, for $z_b \leq 2\delta_u a/(M\lambda)$). Hence, both quantities depend on the object position z_b as well as on the object features (a and d).

The density plot in fig. 4(c) reports the visibility $V(d/\Delta x^f, z_b - z_a)$ of the refocused correlation plenoptic images of double-slit masks, evaluated in the present experimental setup. Besides giving the degree of reliability of the geometrical prediction of eq. (3), this plot unveils the physical limit of resolution and DOF in CPI. The comparison of the two results (dashed line and density plot) indicates that the range of perfect refocusing obtained by eq. (3) is slightly optimistic, but gives a reliable indication of the general behavior of the maximum achievable DOF enabled by CPI. To compare CPI with both
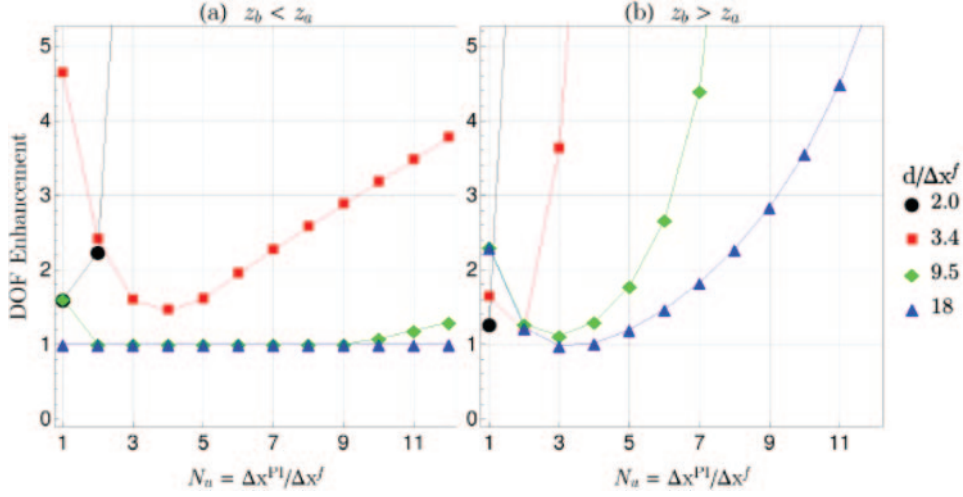
Fig. 5. – Comparison between standard PI and CPI in terms of their maximum achievable DOF *vs.* resolution for double slits of varying distance d, and width $a = d/2$. The DOF is evaluated by considering the maximum (z_b^M) and the minimum (z_b^m) values of the object distance for which the image is still resolved based on Rayleigh criterion (namely, $V \geq 10\%$). We report the results for (a) $z_b < z_a$, and (b) $z_b > z_a$ obtained by considering the experimental setup for CPI, and an equivalent standard PI device.

standard imaging and standard PI, we consider the corresponding imaging devices having the same NA as the light source in our experiment, and report in figs. 4(a) and (b) the visibility they achieve[2]. For standard PI, we have considered $N_u = 3$ to avoid strongly compromising the image resolution. Comparison of figs. 4(a), (b) and (c) indicates that CPI combines at best the advantages of standard imaging and plenoptic imaging: It preserves the resolution of standard imaging while increasing the DOF even beyond the typical values of standard PI. Interestingly, for close up $(z_b < z_a)$, object details larger than $d \gtrsim \sqrt{8\lambda z_a} \simeq 2.8\Delta x^f$ (*i.e.*, the refocusing limit corresponding to $z_b = z_a/2$) can always be refocused by CPI, no matter how close the object is to the source[3]. For $z_b > z_a$, the maximum achievable depth of field is limited, but still significantly larger than in both standard imaging and standard PI. Hence, CPI tends to reach the fundamental limits imposed by the wave nature of light to both image resolution and DOF. From fig. 4, one can also infer that the double-slits associated with the experimental points A, B and C can only be refocused by CPI, as demonstrated in fig. 2. In particular, the object corresponding to the experimental points A and B can be refocused by CPI in a range three times larger than in standard imaging, and twice larger than in a standard PI device characterized by a three times worse spatial resolution. The wider double-slit corresponding to the experimental point C has twice the DOF of standard imaging, and a slightly wider DOF than in standard PI with $N_u = 3$.

---

[2] In these cases, the defocusing distance $z_b - z_a$ represents the distance of the object (placed in z_b) from the conjugate image plane (*i.e.*, $z_a = s_o$ satisfies the thin lens equation $1/s_o + 1/s_i = 1/f$, where s_i is the distance of the lens from the image, and f is the lens focal length).

[3] Of course, the sensor S_a must be sufficiently large to contain such magnified images.

In order to summarize the above results, in fig. 5, we plot the ratio between the maximum achievable DOF of CPI and standard PI (called "DOF enhancement"), as a function of the ratio between their maximum image resolutions (which corresponds to the number of angular pixels N_u of standard PI). All parameters are the same employed to obtain fig. 4. To better emphasize the lack of refocusing limit for close up, we have chosen to separately plot the two cases of object closer to and farther from the conjugate plane $z_b = z_a$. CPI is seen to significantly overcome the DOF of both standard imaging (corresponding to $N_u = 1$) and standard plenoptic imaging, while maintaining the diffraction-limited resolution of standard imaging. In line with the results in fig. 4, the DOF of standard PI and CPI are equal only for $z_b < z_a$, when large enough objects and N_u are considered. Figure 5 also indicates how the number of angular pixels per microlens (N_u) affects the DOF of standard PI, for different object details.

4. – Conclusions and outlook

We have shown that correlation measurements performed on a chaotic light source enable to push plenoptic imaging toward the fundamental limit imposed by wave optics on resolution and DOF; in particular, CPI has been shown to increase the DOF of standard imaging by a factor of three. Still, unlike standard PI, CPI has no limits on the image resolution, which remains diffraction-limited as in standard imaging systems (fig. 4). The advantages of both standard and plenoptic imaging are thus combined at best in CPI, whose maximum achievable DOF is solely limited by interference and diffraction effects [29]. Therefore, CPI has the potential to strongly improve the performances of both microscopy, where high lateral and axial resolutions are required, and 3D imaging, where fast multiperspective acquisitions are desired. Interestingly, plenoptic imaging is the first application in which the surprising simultaneous correlation in both position and momentum, typical of both chaotic and entangled systems, is effectively used to beat intrinsic limits of standard imaging systems.

REFERENCES

[1]   ADELSON E. H. and WANG J. Y., *IEEE Trans. Pattern Anal. Machine Intell.*, **14** (1992) 99.
[2]   MUENZEL S. and FLEISCHER J. W., *Appl. Opt.*, **52** (2013) D97.
[3]   LEVOY M. and HANRAHAN P., *Light field rendering*, in *Proceedings of the 23rd Annual Conference on Computer Graphics and Interactive Techniques* (ACM) 1996, pp. 31–42.
[4]   LEVOY M., NG R., ADAMS A., FOOTER M. and HOROWITZ M., *ACM Trans. Graph. (TOG)*, **25** (2006) 924.
[5]   BROXTON M., GROSENICK L., YANG S., COHEN N., ANDALMAN A., DEISSEROTH K. and LEVOY M., *Opt. Express*, **21** (2013) 25418.
[6]   GLASTRE W., HUGON O., JACQUIN O., DE CHATELLUS H. G. and LACOT E., *Opt. Express*, **21** (2013) 7294.
[7]   PREVEDEL R., YOON Y.-G., HOFFMANN M., PAK N., WETZSTEIN G., KATO S., SCHRÖDEL T., RASKAR R., ZIMMER M., BOYDEN E. S. *et al.*, *Nat. Methods*, **11** (2014) 727.
[8]   FAHRINGER T. W., LYNCH K. P. and THUROW B. S., *Meas. Sci. Technol.*, **26** (2015) 115201.
[9]   HALL E. M., THUROW B. S. and GUILDENBECHER D. R., *Appl. Opt.*, **55** (2016) 6410.
[10] WU C. W., *The Plenoptic Sensor*, PhD Thesis, University of Maryland, College Park (2016).

[11] Lv Y., Wang R., Ma H., Zhang X., Ning Y. and Xu X., *Med. Phys.*, **43** (2016) 3679.
[12] Wu C., Ko J. and Davis C. C., *Opt. Lett.*, **41** (2016) 3169.
[13] Wu C., Ko J. and Davis C. C., *Opt. Express*, **24** (2016) 11975.
[14] Raytrix GmbH, `https://raytrix.de/`.
[15] Ng R., Levoy M., Brédif M., Duval G., Horowitz M. and Hanrahan P., *Comput. Sci. Tech. Report CSTR*, **2** (2005) 1.
[16] Xiao X., Javidi B., Martinez-Corral M. and Stern A., *Appl. Opt.*, **52** (2013) 546.
[17] Shademan A., Decker R. S., Opfermann J., Leonard S., Kim P. C. and Krieger A., *Plenoptic cameras in surgical robotics: Calibration, registration, and evaluation*, in *Proceedings of 2016 IEEE International Conference on Robotics and Automation (ICRA)* (IEEE) 2016, pp. 708–714.
[18] Le H. N., Decker R., Opferman J., Kim P., Krieger A. and Kang J. U., *3-d endoscopic imaging using plenoptic camera*, in *Proceedings of CLEO: Applications and Technology* (Optical Society of America) 2016, pp. AW4O–2.
[19] Carlsohn M. F., Kemmling A., Petersen A. and Wietzke L., *3d real-time visualization of blood flow in cerebral aneurysms by light field particle image velocimetry*, in *Proceedings of SPIE Photonics Europe* (International Society for Optics and Photonics) 2016, p. 989703.
[20] D'Angelo M., Pepe F. V., Garuccio A. and Scarcelli G., *Phys. Rev. Lett.*, **116** (2016) 223602.
[21] Pepe F. V., Scarcelli G., Garuccio A. and D'Angelo M., *Quantum Meas. Quantum Metrol.*, **3** (2016) 20.
[22] Pepe F. V., Di Lena F., Garuccio A., Scarcelli G. and D'Angelo M., *Technologies*, **4** (2016) 17.
[23] Pittman T., Fitch M., Jacobs B. and Franson J., *Phys. Rev. A*, **68** (2003) 032316.
[24] Gatti A., Brambilla E., Bache M. and Lugiato L. A., *Phys. Rev. Lett.*, **93** (2004) 093602.
[25] D'Angelo M. and Shih Y., *Laser Phys. Lett.*, **2** (2005) 567.
[26] Valencia A., Scarcelli G., DAngelo M. and Shih Y., *Phys. Rev. Lett.*, **94** (2005) 063601.
[27] Scarcelli G., Berardi V. and Shih Y., *Phys. Rev. Lett.*, **96** (2006) 063602.
[28] Ferri F., Magatti D., Gatti A., Bache M., Brambilla E. and Lugiato L., *Phys. Rev. Lett.*, **94** (2005) 183602.
[29] Pepe F. V., Di Lena F., Mazzilli A., Edrei E., Garuccio A., Scarcelli G. and DAngelo M., *Phys. Rev. Lett.*, **119** (2017) 243602.